Lift force acting on an intruder in dense, granular shear flows

Meng Liu and Christoph R. Müller[*]

Department of Mechanical and Process Engineering, ETH Zürich, Leonhardstrasse 21, 8092 Zürich, Switzerland

We report a lift force model for intruders in dense, granular shear flows. Our derivation is based on the thermal buoyancy model of Trujillo and Hermann [Physica A **330**, 519 (2003)], but it takes into account both granular temperature and pressure differences in the derivation of the net buoyancy force acting on the intruder. In a second step, the model is extended to take into account also density differences between the intruder and the bed particles. The model predicts very well the rising and sinking of intruders, the lift force acting on intruders as determined by discrete element model simulations, and the neutral-buoyancy limit of intruders in shear flows. Phenomenologically, we observe a cooling upon the introduction of an intruder into the system. This cooling effect increases with intruder size and explains the sinking of large intruders. On the other hand, the introduction of small to midsized intruders, i.e., up to four times the bed particle size, leads to a reduction in the granular pressure compared to the hydrostatic pressure, which in turn causes the rising of small to midsized intruders.

I. INTRODUCTION

Since the first report by Brown [1], segregation effects in granular systems have received widespread interest among both physicists and engineers due to their high practical relevance. Particles of different sizes [2], densities [3], and possibly also shapes [4] segregate when excited, e.g., via vibration, rotation, or gas injection. Segregation is readily encountered in many processing apparatuses such as rotating cylinders [5], hoppers [6], or vibrated beds [2]. In industrial applications, segregation is typically an undesirable effect as it counteracts mixing. In addition, segregation in granular media is also commonly observed in nature, e.g., rock avalanches and debris flow [7,8]. Arguably, model systems in which one or multiple intruders are immersed in a granular bed have been studied most frequently, and in such systems the so-called "Brazil nut phenomenon" (BNP) has been reported. In the BNP, which is not limited to single intruders, a larger particle rises through a bed of smaller particles under external excitation, typically vibration. Depending on the regularity of the vibrational excitation, the BNP has been explained by percolation [2,9] or convection [10]. The percolation model explains the rising of a larger intruder through a bed of smaller particles via a void filling mechanism. During a vibration cycle, first a void is formed underneath the intruder. This void is subsequently filled by the small, surrounding bed particles. At the end of a vibration cycle, the intruder falls back to a higher rest position. Through a geometric description of the percolation model, Duran *et al.* [9] predicted that the rise velocity of the intruder depends on the size ratio of the intruder to the bed particles. For very regular vibrations, a convective flow field is established that carries the intruder upwards until it reaches the surface of the bed. The intruder is trapped at the surface as

the region close to the walls where downwards motion occurs is typically smaller than the intruder. In this model, the rise velocity of the intruder is independent of the ratio of the size of the intruder to the bed particles. Although, the two models described above provide some conceptual understanding of segregation in granular media, there is still considerable debate on how to model segregation from a continuum perspective. Such continuum models require formulations of the granular counterparts of drag, buoyancy, and in specific cases the Saffman forces.

Using discrete element method (DEM) simulations, Shishodia and Wassgren [11] were among the first to establish an expression for the buoyancy force in a granular system. In their two-dimensional (2D) vibrofluidized bed simulations, periodic boundary conditions were employed to eliminate the contribution of convection. In the absence of a convective pattern, the intruder was found to rise to an equilibrium position within the bed (bed position y) instead of rising to the top. Making an analogy to the fluid mechanic description of the buoyancy force, i.e., the product of a pressure gradient and the intruder volume, Shishodia and Wassgren proposed the following expression for the buoyancy force, F_b:

$$\mathbf{F}_b = \nabla P(y) V_I = -m_I g, \tag{1}$$

where $m_I \mathbf{g}$ is the weight of the intruder, $\nabla P(y)$ is the pressure gradient, and V_I is the intruder volume.

It is worth noting that the 2D granular system investigated by Shishodia and Wassgren [11] was in the granular gas regime in which binary particle collisions dominate. When considering practically more relevant dense granular systems in which multiparticle collisions and long-lasting contacts dominate, the buoyancy force predicted through Eq. (1) underestimates the measured buoyancy force acting on the intruder when the intruder size approaches the size of the bed particles [12].

---

[*]Corresponding author: muelchri@ethz.ch

On the other hand, Trujillo and Herrmann [13] developed a granular buoyancy model using the kinetic theory of granular gases. The system considered contained a single intruder in a vibrated bed. The driving force acting on the rising intruder was modeled as a thermal-induced buoyancy force, i.e., a density difference arising from differences in the granular temperature of the system with and without the intruder. In their model, a reference state "0" was defined that is characterized by a granular pressure $P_0(\mathbf{r})$ and temperature $T_0(\mathbf{r})$, where $\mathbf{r}$ is the position of the intruder. The reference state assumes a bed without the intruder. Upon introduction of the intruder, the bed transitions to a new state "1" which is characterized by $P_1(\mathbf{r})$ and $T_1(\mathbf{r})$. The temperature difference between the "perturbed" and reference states is given as $\Delta T(\mathbf{r}) = T_1(\mathbf{r}) - T_0(\mathbf{r})$, yielding the following expression for a granular, thermally induced buoyancy force [13]:

$$F_b = \alpha \Delta T \rho V_I g, \qquad (2)$$

with ρ being the bulk density of the reference state (i.e., $\rho = \rho_p \phi$, with ρ_p being the density of the bed particles and ϕ being the solid fraction of the bed), g is the acceleration due to gravity, and α is the coefficient of thermal expansion, defined as $\alpha = -\frac{1}{n}(\frac{\partial n}{\partial T})_P$, where n is the number density of the bed particles. Assuming α to be constant, Trujillo and Herrmann showed that $\alpha = \frac{1}{T_0} C(\phi)$, where $C(\phi)$ depends on the solid fraction with $C(\phi) \to 1$ for $\phi \to 0$. The system considered by Trujillo and Hermann [13] was a vibrofluidized bed and a uniform system pressure i.e., $dP \sim 0$ was assumed. However, such a simplification would not be valid in dense, shear systems (*vide infra*).

To summarize, the buoyancy models described in Eqs. (1) and (2) have been developed for systems that operate in the granular gas regime. However, when considering more "liquidlike," dense granular systems, additional effects have to be considered in the buoyancy model. For example, in an experimental study of a dense, vertically vibrated bed (amplitude $A = 9.76$ mm and frequency $f = 9.7$ Hz), Shinbrot and Muzzio [14] observed that intruders ($d_I = 152$ mm) with a density $<0.5\rho_p$ sink, whereas heavy intruders ($d_I = 152$ mm) with a density in the range 1.2–1.7ρ_p rise. This unexpected behavior has been termed the reverse Brazil nut phenomenon (RBNP). As the intruder size was fixed in these two experiments, the buoyancy model described in Eq. (1) cannot explain why the heavier intruder rises to the top while the lighter intruder sinks. It has been argued that the interstitial air in beds of small particles ($<800\,\mu$m) might contribute to the RBNP [14]. To weaken the influence of the interstitial gas in a vibrated bed, Huerta *et al.* [12] investigated the BNP in a dense bed containing larger particles (i.e., a mixture of glass beads 3 and 4 mm in diameter). Huerta *et al.* [12] observed that a light intruder rises faster than a heavier intruder of equal size. Unlike in the setup of Shinbrot and Muzzio [14], the bed of Huerta *et al.* [12] was vibrated horizontally with neighboring sidewalls vibrating with the same amplitude but out of phase (phase shift π), ensuring the cross-sectional area of the bed to remain almost constant over a vibration cycle and avoiding in turn the establishment of a convection pattern. Huerta *et al.* [12] measured the lift force acting on the intruder by connecting the intruder, placed in the center of the bed, with a force sensor. The measured lift force $\mathbf{F}_{\text{lift}} = -(\mathbf{F}_s + \mathbf{F}_g)$,

where $\mathbf{F}_g$ is the gravitational force of the intruder and $\mathbf{F}_s$ is the time-averaged value obtained from the force sensor, can be interpreted as the buoyancy force acting on the intruder. The measured lift force was fitted to a generalized Archimedean formulation of the buoyancy force, viz.,

$$F_b = |\mathbf{F}_s + \mathbf{F}_g| = \rho_p \phi V_I g, \qquad (3)$$

where the "fitting constant" ϕ was very close to the average solid fraction of the bed, i.e., the intruder rises as in a fluid with a density that is equal to the bulk density of the granular media ($\phi \rho_p$). However, the experimental data acquired by Huerta *et al.* [12] showed only good agreement with the buoyancy model given by Eq. (3) for large ($d_I/d_p > 4$) and very light intruders ($\rho_I/\rho_p = 0.0169$). As the intruder size approached the size of the bed particles, the measured buoyancy force exceeded the predictions of the generalized Archimedean principle given in Eq. (3). In a convection-free, vibrated bed in which the intruder is fixed in an equilibrium position and only buoyancy and gravity forces are acting on the intruder, the buoyancy force will become smaller than the bed particle weight for $V_I \to V_p$, i.e., $F_b = \phi \rho_p V_p g < m_p g$ as the solid fraction of the bed $\phi < 1$. Thus, the generalized Archimedean principle expressed in Eq. (3) underestimates the buoyancy force acting on a bed particle. This limitation of the buoyancy model given in Eq. (3) has also been remarked upon by van der Vaart *et al.* [15].

Although the buoyancy concept was investigated initially in vibrated systems, its applicability to shear flow systems of practical relevance has also been studied. Qualitatively, Savage and Lun [16] proposed that in dense shear flows, segregation is driven by both kinetic sieving and squeeze expulsion. Overall, there is a higher probability of finding a void into which a small particle can fall compared to a void into which a large particle can fall. This size-dependent, gravity-induced segregation mechanism has been termed "random fluctuating sieving" or "kinetic sieving." In addition, a force imbalance on a particle leads to the particle being squeezed out of its layer. This mechanism was termed "squeeze expulsion," but it is neither necessarily size dependent nor does it have a preferred direction. However, there is currently no continuum model that describes accurately the motion of segregating intruder(s) in dense, granular shear flows. To gain some insight into these systems, Guillard *et al.* [17] performed 2D, steady-state, shear-flow simulation using DEM to quantify the lift force acting on an intruder as a function of the prevailing pressure (and stress) gradient. The size of the intruder was varied from d_p to $10\,d_p$ while fixing the intruder density to the density of the bed particles. In their simulations, the intruder was kept at a position of half the height of the bed ($h_c/2$) by connecting it to a virtual spring. The virtual spring imposed an additional (spring) force onto the intruder, i.e., $\mathbf{F}_s = -k_s(y_1 - y_0)\mathbf{e}_y$, where k_s is the spring constant, y_1 is the vertical position of the intruder at a given time, $y_0 = h_c/2$ is the initial position of the intruder, and $\mathbf{e}_y$ is the unit vector in the y direction. The virtual spring ensures that the intruder remains at its equilibrium position while allowing its free movement along the direction of the flow. The buoyancy force acting on the intruder was calculated in analogy to Eq. (1) and expressed as a function of the spatial gradients of the granular

pressure and shear, viz.,

$$F_{\text{lift}} = -\pi \frac{d_I}{4}\left(F(\mu, d_I/d_p)\frac{\partial P}{\partial y} + G(\mu, d_I/d_p)\frac{\partial |\tau|}{\partial y}\right), \quad (4)$$

where τ is the granular shear stress, P is the granular pressure, and $\mu = |\tau|/P$ is the bulk friction coefficient. Guillard *et al.* [17] proposed the factors F and G to be exponential functions of μ and d_I/d_p.

In a subsequent study, van der Vaart *et al.* [15] aimed to elucidate whether the lift force acting on an intruder in a shear flow can be expressed as the sum of a granular buoyancy force and a Saffman-type lift force, i.e.,

$$F_{\text{lift}} = F_{\text{b}} + F_{\text{Saff}}. \quad (5)$$

where $F_{\text{Saff}} = -a_0 b_0 I_\theta \mu^{-0.5}(d_p/d_I - 1)d_I^2 d_p^{-1}\text{sgn}(\dot{\gamma})$ [a_0 and b_0 are fitting constants, $I_\theta = \dot{\gamma}d_p/(P/\rho_p)^{0.5}$, $\dot{\gamma}$ is the shear rate, and μ is the bulk friction coefficient]. Van der Vaart *et al.* [15] considered a full 3D, dense shear flow along an inclined plane with an inclination angle θ with respect to the horizontal direction. Van der Vaart *et al.* [15] modified Eq. (3) to correct for the underestimation of the buoyancy force for $V_I \rightarrow V_p$ by replacing the solid fraction of the bed, ϕ, by ϕ/ϕ_I, where ϕ_I is the solid fraction of the intruder, yielding

$$F_{\text{b}} = \rho_p \frac{\phi}{\phi_I}V_I g. \quad (6)$$

The solid fraction of the intruder is defined as the ratio of its Voronoi volume, $\tilde{V}_I$, to its physical volume, V_I. The modified buoyancy model Eq. (6) has also recently been assessed and validated in a vibrofluidized system [18]. The derivation of the Saffman lift force is limited to conditions in which inertia is not dominating the local flow around the intruder, i.e., when the shear rate-based Reynolds number Re $\ll 1$. Furthermore, it is currently unclear whether the Saffman lift force model also holds for very large intruders which have been found to sink [19].

In the most recent work, Jing *et al.* [20] reported a simple buoyancy-based model to describe the lift force acting on a single spherical intruder in a dense, granular shear flow. By varying the size and density ratio of the intruder to bed particles, it was found that the lift force F_{lift}, as determined via a virtual spring, i.e., $\mathbf{F}_{\text{lift}} = -(\mathbf{F}_s + \mathbf{F}_g)$, collapses onto an Archimedean-type model, viz.,

$$F_{\text{b}} = f(D)\,\rho_p \phi V_I g, \quad (7)$$

where $f(D) = [1 - c_1\exp(-D/a_1)][1 + c_2\exp(-D/a_2)]$ is a fitting function with fitting constants $c_1 = 1.43$, $c_2 = 3.55$, $a_1 = 0.92$, $a_2 = 2.94$, and $D = d_I/d_p$. As for $D \gg 1$, $f(D) \rightarrow 1$, the observation that with increasing D the lift force approaches the generalized Archimedean principle [Eq. (3)] is captured by Eq. (7). This trend of the buoyancy force for $D \gg 1$, which can be considered as the continuum limit, can be explained as follows. As the surface area of the intruder increases with D^2, the number of contacts between the intruder and the surrounding bed particles increases rapidly with increasing D, yielding a uniform stress transmission to the intruder for $D \gg 1$ and hence a similar behavior to that of an intruder immersed in a fluid. On the other hand, for $D \rightarrow 1$, the stress distribution on the intruder is highly anisotropic, leading to a deviation from Eq. (3).

However, the effect of stress anisotropy on the lift force acting on an intruder remains largely unclear. Nonetheless, despite the empirical derivation of $f(D)$, Eq. (7) can be of practical importance, allowing us to make an *a priori* prediction of whether an intruder of a given size and density ratio will sink or rise.

To summarize, recent works have improved significantly our understanding of size-driven segregation of intruders in dense shear flows and its continuum modeling. However, although several works observe a distortion of the hydrostatic pressure field, in addition to the granular temperature field, upon the addition of the intruder, the model of Trujillo and Hermann [13] is limited to disturbances in the temperature field, which is most likely insufficient to describe dense granular systems. Furthermore, while the theoretical models have been shown to predict well the forces acting on intruders for lower ratios of d_I/d_p (e.g., $d_I/d_p < 4$ for [15]), theoretical models that can also predict accurately the sinking of very large intruders would be advantageous. Hence, in this work we aim to extend the original work of Trujillo and Hermann [13] to dense shear flow systems by describing local perturbations in both the pressure and temperature field upon the introduction of an intruder. Compared to existing models for the lift force acting on an intruder, the model proposed here is based on a physical description of the granular system. The proposed model not only predicts quantitatively the lift force acting on the intruder, but it also provides insight into the mechanisms at play.

II. METHOD

A. Simulation method

DEM simulations of the shear flow system considered here were performed using the LIGGGHTS software [21]. In DEM, each particle is modeled as a single entity (Lagrangian approach) and the normal, $F_{n,\alpha\beta}$, and tangential contact forces, $F_{t,\alpha\beta}$, acting between the contacting particles α and β are modeled by a Hertzian contact model [22,23]:

$$F_{n,\alpha\beta} = -k_n\sqrt{\frac{1}{4R^*}}\delta_{n,\alpha\beta}^{3/2} + \gamma_{n,\alpha\beta}\sqrt{m^*}\sqrt[4]{\frac{\delta_{n,\alpha\beta}}{4R^*}}u_{n,\alpha\beta}, \quad (8)$$

$$F_{t,\alpha\beta} = -k_t\sqrt{\frac{1}{4R^*}}\delta_{t,\alpha\beta}^{3/2} + \gamma_{t,\alpha\beta}\sqrt{m^*}\sqrt[4]{\frac{\delta_{t,\alpha\beta}}{4R^*}}u_{t,\alpha\beta}, \quad (9)$$

where k_n and k_t are the spring constants in the normal and tangential direction, respectively. Here, δ_n and δ_t are the particle overlaps in, respectively, the normal and tangential direction, γ_n and γ_t are the damping coefficients in, respectively, the normal and tangential direction, R^* is the effective radius given as $R^* = R_\alpha R_\beta/(R_\alpha + R_\beta)$, $m^* = m_\alpha m_\beta/(m_\alpha + m_\beta)$, and $u_{n,\alpha\beta}$ and $u_{t,\alpha\beta}$ are the tangential and normal relative velocities between particles α and β, respectively. The tangential contact force, $F_{t,\alpha\beta}$, is limited by Coulomb's law, i.e., $F_{t,\alpha\beta} \leqslant \mu F_{n,\alpha\beta}$, with μ being the coefficient of friction.

We have chosen to study inclined plane flow as it is one of the classical setups, having well-established flow dynamics [24]. Figure 1 illustrates the setup of the simulation domain. The bed of dimensions $lx \times lz \times h_c = 20d_p \times 20d_p \times 40d_p$ consists of 16 000 bed particles of diameter d_p. We have
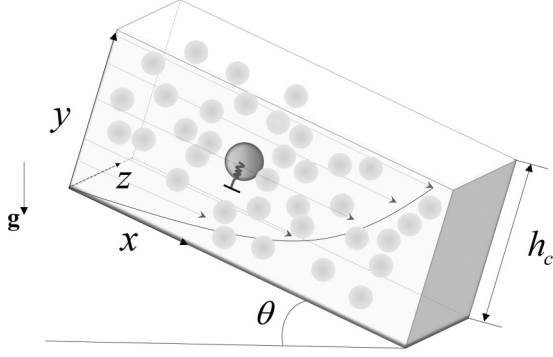
FIG. 1. Sketch of the granular shear flow system under investigation. An intruder (dark gray) is immersed in the bed at an initial location $y_0 = h_c/2$. The inclination angle is given by θ, and h_c is the distance (in the y-direction) from the bottom of the bed to its surface. For simplicity, we introduce a local coordinate system. A virtual spring (blue spring) is attached to the intruder. The intruder is able to move freely in the xz plane, while it reaches a (dynamic) equilibrium position y_1. The size of the simulation domain is $lx \times lz \times h_c = 20d_p \times 20d_p \times 40d_p$.

confirmed that the computational domain is adequately sized since doubling its size had no effect on the numerical results. The bed particles flow along an inclined plane due to gravity. The gravitational vector $|\mathbf{g}| = 9.81 \, m/s^2$ can be decomposed into $\mathbf{g}_x = \mathbf{g} \sin\theta$ and $\mathbf{g}_y = \mathbf{g} \cos\theta$. Particles with a diameter $d_w = 10 \, mm$ are glued onto the bottom plate to increase the roughness of the bottom wall. In the x and z directions, periodic boundaries were applied to establish a steady-state shear flow. The velocity profiles in the shear flow were varied by adjusting the inclination angle θ. However, as only a narrow range of θ ensures steady-state conditions, the inclination angle θ was only varied in the range $24° \leqslant \theta \leqslant 28°$ in this work. The inclined chute flow is chosen due to its well-established dynamics. A spherical intruder of diameter d_I was placed inside the bed at a vertical position $y_c = h_c/2 = 20d_p$. The motion of the intruder in the y-direction was constrained by a virtual spring (spring constant 80 N/m). The spring constant has been varied by a factor of 4, and we have observed a negligible effect on the lift force. The intruder can move freely in the xz plane. The spring force acting on the intruder is determined through its displacement in the y direction, i.e., $\mathbf{F}_s = -k_s(y - y_0)\mathbf{e}_y$. The vertical displacement of the intruder is very small, at most $0.5d_p$ for $d_I/d_p = 8$. The lift force acting on the intruder is then given by $\mathbf{F}_{\text{lift}} = -(\mathbf{F}_s + \mathbf{F}_g)$. The parameters used in the DEM simulation are given in Table I. The reported parameters correspond to the material properties of glass, except for the particle spring constant for which a lower value was chosen to accommodate DEM simulation constraints.

B. Coarse-graining

To obtain the granular pressure, stress, and temperature, coarse-graining (CG) of the DEM data was employed [25,26]. The granular stress tensor in the coarse-graining volume is

TABLE I. Parameters used in the DEM simulations.

Parameters	Value
k_n (N/m)	6.41×10^4
k_t (N/m)	$2/7k_n$ [24]
d_p(m)	0.005
d_I(m)	d_p up to $\sim 8d_p$
d_w(m)	0.01
ρ_p(kg/m^3)	2500
γ_n[(N/m)$^{1/2}$]	23.01 [24]
γ_t[(N/m)$^{1/2}$]	$1/2\gamma_n$
μ	0.5
e	0.88
Time step (s)	10^{-5}

given by [27]

$$\sigma_{i,j}(\mathbf{r}, t) = -\frac{1}{2} \sum_{\alpha,\beta} f_{i,\alpha\beta} r_{j,\alpha\beta} \int_0^1 \Phi(r - \mathbf{r}_\alpha + s\mathbf{r}_{\alpha\beta}) ds$$

$$- \sum_{\alpha=1}^N m_\alpha \Phi(\mathbf{r} - \mathbf{r}_\alpha) u'_{i,\alpha} u'_{j,\alpha}, \quad (10)$$

where Φ is the coarse-graining function, i, j denotes the Cartesian components, $f_{i,\alpha\beta}$ is the ith component of the contact force vector between particles α and β (see the illustration in Fig. 2), and $r_{j,\alpha\beta}$ is the branch vector connecting the centers of gravity of particles α and β. We use the Heaviside function as the coarse-graining function, i.e., $\Phi(\mathbf{R}) = 1/(4/3\pi w^3)H(w - |\mathbf{R}|)$, where w is the radius of the spherical coarse-graining volume, $\mathbf{R} = \mathbf{r} - \mathbf{r}_\alpha$ is the vector pointing from a sampling particle inside the coarse-graining volume to the center ($\times$) of the coarse-graining volume, and $u'_{i,\alpha}$ is the velocity fluctuation of particle α, viz., $u'_{i,\alpha} = u_{i,\alpha} - \bar{u}_i$, where $u_{i,\alpha}$ is the instantaneous velocity of particle α in the ith
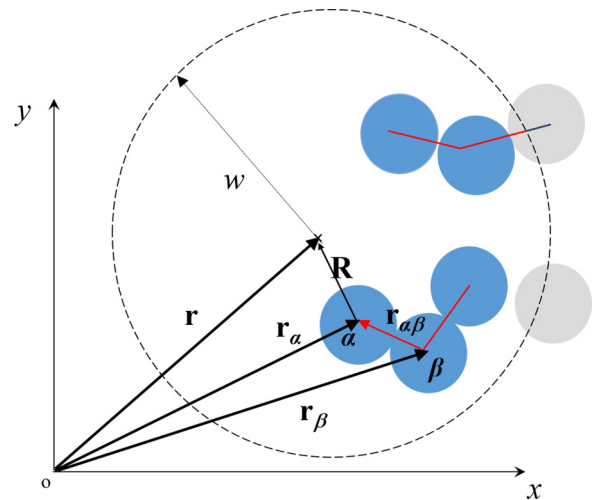

FIG. 2. Illustration of the coarse-graining method. The coarse-graining volume is bounded by a spherical space centered at $\mathbf{r}$ with the coarse-graining radius w. The branch vector $\mathbf{r}_{\alpha\beta} = \mathbf{r}_\alpha - \mathbf{r}_\beta$ is shown as a red arrow that points from particle β to particle α.
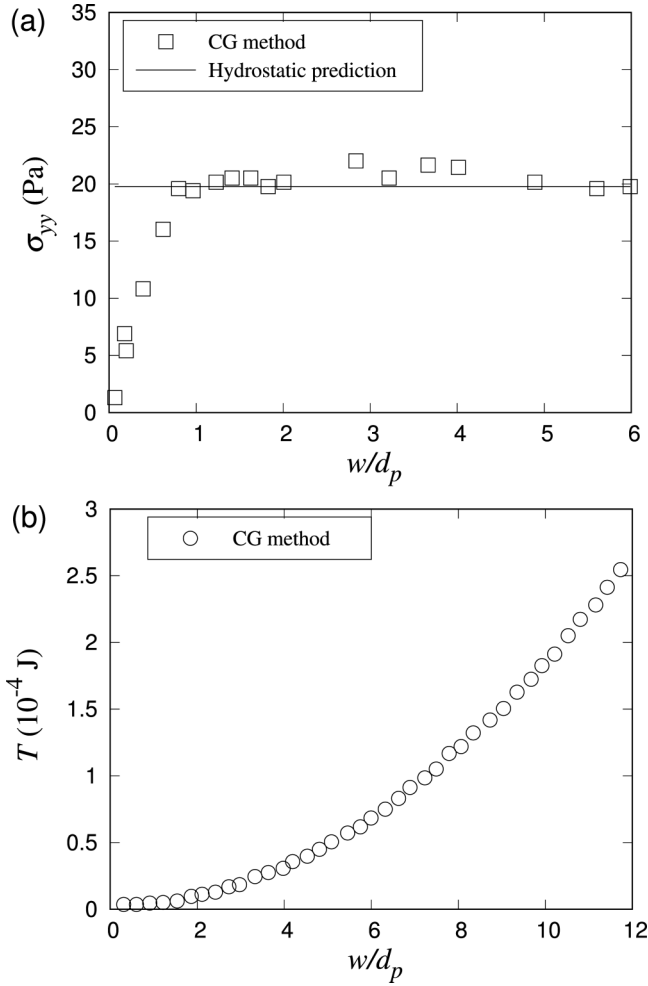
FIG. 3. Dependence of σ_{yy} and the granular temperature on the normalized coarse-graining radius w/d_p: (a) σ_{yy} increases with increasing w/d_p for $w/d_p < 1$. For $w \geqslant d_p$, σ_{yy} reaches an asymptotic value that is in excellent agreement with its hydrostatic value, i.e., $Nm_p g/(lx \cdot lz)$, where N is the particle number, m_p is the particle mass, and $lx \cdot lz$ is the cross-sectional area of the system. (b) The granular temperature increases continuously with increasing coarse-graining radius w/d_p.

direction, and $\bar{u}_i$ is the average velocity in the ith direction of the particles in the coarse-graining volume.

The average pressure in the coarse-graining volume is given by $P = 1/3(\sigma_{ii} + \sigma_{jj} + \sigma_{kk})$. The value of $\sigma_{i,j}$ depends mainly on the coarse-graining radius w. For example, Fig. 3(a) shows the dependence of σ_{yy} on the coarse-graining radius w. For $w/d_p < 1$, σ_{yy} increases with increasing w/d_p, but it reaches an asymptotic value for $w/d_p \geqslant 1$, in agreement with previous works [26,28]. To avoid an oversmoothing of the local stresses, we chose $w = \bar{d} = 1/2(d_I + d_p)$, in agreement with previous works [15,29,30].

Turning now to the granular temperature, viz. [13,31],

$$\frac{3}{2}T = \frac{1}{N}\sum_{\alpha=1}^{N}\frac{1}{2}m_\alpha(u_{i,\alpha}'^2 + u_{j,\alpha}'^2 + u_{k,\alpha}'^2), \qquad (11)$$

where i, j, and k denote the Cartesian components, $u_{i,\alpha}'$, $u_{j,\alpha}'$, $u_{k,\alpha}'$ are, respectively, the velocity fluctuations of particle α

with regard to the respective average velocity in the coarse-graining volume. The magnitude of the granular temperature depends on the coarse-graining volume. For example, in the dense granular shear flow system studied here, the granular temperature increases monotonically with increasing coarse-graining volume [Fig. 3(b)]. Recently, a method has been proposed to eliminate the influence of the coarse-graining volume on the granular temperature, however the approach is only suitable for very specific systems such as monodisperse shear flows [28]. However, as this work concentrates on the effect of a differently sized granular intruder on the granular temperature of the system when compared to the intruder-free reference case, this method is not applicable to the system studied here. Generally, there is very little consensus on the "correct" coarse-graining radius for the granular temperature [32]. In the work of Trujillo and Hermann [13], a coarse-graining radius of $w = L/3$ (L is the width of the vibrating bed) was chosen for the granular temperature calculation to achieve a good agreement between their thermal buoyancy model and the experimental measurements. Here, we have decided to use the coarse-graining radius $w = r_I + d_p$ for the granular temperature, as it is physically reasonable to include the first layer of particles around an intruder into the coarse-graining radius.

III. MODEL DESCRIPTION

Hermann [33] proposed a thermodynamic formulation for moving granular media that was subsequently adopted to investigate the BNP problem [13]. First, they defined a reference state of a vibrofluidized bed that is described by a given granular pressure $P_0(\mathbf{r})$ and granular temperature $T_0(\mathbf{r})$. When introducing an intruder into the system, the state at $\mathbf{r}$ changes and is referred to as a perturbed state "1" described by the granular pressure $P_1(\mathbf{r})$ and granular temperature $T_1(\mathbf{r})$. Trujillo and Hermann [13] argued that the perturbed granular system tends to reestablish its reference state, leading to a displacement of the intruder from its initial position $\mathbf{r}$. Neglecting changes in the granular pressure due to the presence of the intruder, Trujillo and Hermann [13] proposed a thermal-driven buoyancy force model [Eq. (2)] to describe the motion of an intruder in a vibrofluidized bed.

In the following, we derive a granular buoyancy model that takes into account also intruder-induced variations in the pressure field to allow the description of the motion of an intruder in a dense, granular shear flow system.

To quantify the impact of an intruder on the local granular temperature and pressure in a shear flow, we consider the two systems (i.e., the reference and perturbed states) illustrated in Fig. 4. Figure 4(a) sketches the shear flow system without an intruder, i.e., the "reference case," while Fig. 4(b) contains an intruder at position $\mathbf{r}$ and is referred to as the "intruder case" (perturbed state). Figure 4(a) is identical to Fig. 4(b) except that the intruder is replaced by bed particles. In the reference case, the granular temperature and pressure at $\mathbf{r}$ (i.e., the center of the imaginary control volume) are referred to as $T_0(\mathbf{r})$ and $P_0(\mathbf{r})$, respectively. Similarly, in the intruder case the granular temperature and pressure at $\mathbf{r}$, i.e., the position where the intruder is located, are denoted as $T_1(\mathbf{r})$ and $P_1(\mathbf{r})$, respectively. $P_0(\mathbf{r})$, $T_0(\mathbf{r})$, $P_1(\mathbf{r})$, and $T_1(\mathbf{r})$ are determined
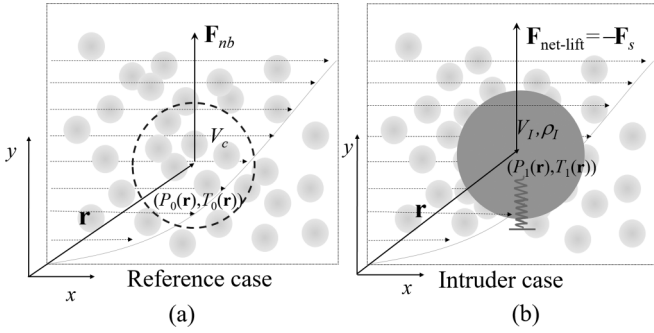
FIG. 4. Illustration of the reference case and the perturbed state, i.e., the shear flow system with the presence of an intruder. (a) Reference case: shear-flow system without the intruder. The intruder is replaced by an imaginary control volume of size $V_c = V_I$, that is filled with bed particles. The boundary of the imaginary control volume is given by a dashed circle. Here, $P_0(\mathbf{r})$ and $T_0(\mathbf{r})$ denote the reference state at $\mathbf{r}$. (b) Perturbed state: intruder of volume V_I and density ρ_I is placed at $\mathbf{r}$ into the shear flow system. $P_1(\mathbf{r})$ and $T_1(\mathbf{r})$ are the granular pressure and temperature at $\mathbf{r}$ in the perturbed state. F_{nb} is the net buoyancy force acting on the control volume, which arises from the temperature and pressure difference between the reference and intruder states. $F_{\text{net-lift}}$ is the force acting on the intruder, which is measured by the (virtual) spring force, $\mathbf{F}_{\text{net-lift}} = -\mathbf{F_s}$, and that keeps the intruder in its equilibrium position. Here, "net" implies that the gravitational force has been subtracted.

through coarse-graining. The change in the system due to the presence of an intruder (compared to the reference state) is described by $\Delta T(\mathbf{r}) = T_1(\mathbf{r}) - T_0(\mathbf{r})$ and $\Delta P(\mathbf{r}) = P_1(\mathbf{r}) - P_0(\mathbf{r})$. We follow now the argumentation of Trujillo and Hermann [13] that the thermodynamic driving force for an intruder to sink or rise (i.e., the lift force acting on the intruder) is related to $\Delta T(\mathbf{r})$ and $\Delta P(\mathbf{r})$. As in our shear flow system, periodic boundary conditions are applied in the x and z directions, and $P(\mathbf{r})$ and $T(\mathbf{r})$ are independent of x and z for a given y, we can simplify our notation to $P(y)$ and $T(y)$.

For an inelastic, hard-sphere system [Fig. 4(a)], the granular pressure can be expressed as [34,35]

$$P = nT\left[1 + \frac{\pi}{3}(1+e)nd_p^3 C(\phi)\right], \quad (12)$$

where n is the particle number density, T is the granular temperature, e is the coefficient of restitution, d_p is the diameter of the particles, ϕ is the solid fraction, and $C(\phi)$ is the pair-correlation function at a contact, i.e., the probability density to find another particle at a distance d_p from a particle center. For a dilute or moderately dense system (i.e., $nd_p^3 \sim 1$), the Carnahan-Starling expression holds, i.e., $C(\phi) = (2 - \phi)/2(1 - \phi)^3$ [27], where Carnahan and Starling [27] assume that binary collisions dominate. This assumption might become inaccurate for denser systems, in which empirical pair correlation functions $C(n)$ that consider multiple particle contacts (as opposed to binary contacts in a granular gas) are required [36,37]. However, for our model, the exact form of Eq. (12) is not relevant as we only utilize the finding that there is a relationship $P = P(n, T)$, and $P = P(n, T)$ can be reformulated as

$$n = n(P, T). \quad (13)$$

Taking the total differential yields

$$dn = \left(\frac{\partial n}{\partial T}\right)_p dT + \left(\frac{\partial n}{\partial p}\right)_T dP = -\alpha n dT + k_p n dP, \quad (14)$$

where α is the thermal expansion coefficient and k_p is the compressibility coefficient, given by

$$\alpha = -\frac{1}{n}\left(\frac{\partial n}{\partial T}\right)_P \quad (15)$$

and

$$k_p = \frac{1}{n}\left(\frac{\partial n}{\partial P}\right)_T. \quad (16)$$

Placing an intruder in the reference shear flow system changes the granular pressure and temperature at position $\mathbf{r}$ from (T_0, P_0) to (T_1, P_1). Assuming α and k_p to be constant and integrating Eq. (14), we obtain

$$n_1 = n_0 e^{(-\alpha \Delta T + k_p \Delta P)}, \quad (17)$$

where $n_0 = N_0/V_c$ is the number density in the reference case (N_0 is the number of particles in the imaginary control volume V_c). The density of the control volume can be expressed as $\rho_0 = (N_0 m_p)/V_c = n_0 m_p$, where m_p is the mass of a bed particle. Using the equivalent expression for ρ_1, i.e., $\rho_1 = n_1 m_p$, we can rewrite Eq. (17) yielding

$$\rho_1 = \rho_0 e^{(-\alpha \Delta T + k_p \Delta P)}. \quad (18)$$

Hence, transitioning from state "0" to "1" leads not only to a change in the granular temperature and pressure (ΔT and ΔP) at position $\mathbf{r}$, but also to a change in density, i.e., $\Delta \rho = (\rho_0 - \rho_1)$. We now make the further assumption that the bulk density outside the control volume region [Fig. 4(a)] is unaffected by the pressure/temperature perturbation (i.e., it is ρ_0). Following Archimedean's principle, we define the net buoyancy force acting on the imaginary control volume in Fig. 4(a) as

$$F_{nb} = (\rho_0 - \rho_1)V_I g_y. \quad (19)$$

As our derivation starts from Eq. (12), which only holds for monodisperse particle systems, the net buoyancy force given in Eq. (19) that is acting on the imaginary control volume in Fig. 4(a) is not expected to be the exact equivalent of the lift force acting on the intruder, but it is expected that there exists a strong correlation between F_{nb} and $F_{\text{net-lift}}$, which will be demonstrated in the following.

Substituting Eq. (18) into Eq. (19), and replacing ρ_0 with $\rho_p \phi$, we obtain the following expression for the net buoyancy force:

$$F_{nb} = (1 - e^{-\alpha \Delta T + k_p \Delta P}) \rho_p \phi V_I g_y. \quad (20)$$

Further, in a steady-state, dense, granular shear flow, the granular pressure at a given height y is given by [39,40]

$$P(y) = (\partial P/\partial y)(y - h_c) = \rho_p \phi g_y (h_c - y), \quad (21)$$

where h_c is the height of the flowing layer. The linear relationship between P and y is confirmed in Fig. 5(a). Substituting now $\phi = nV_p$ in Eq. (21) and combining it with Eq. (16), we
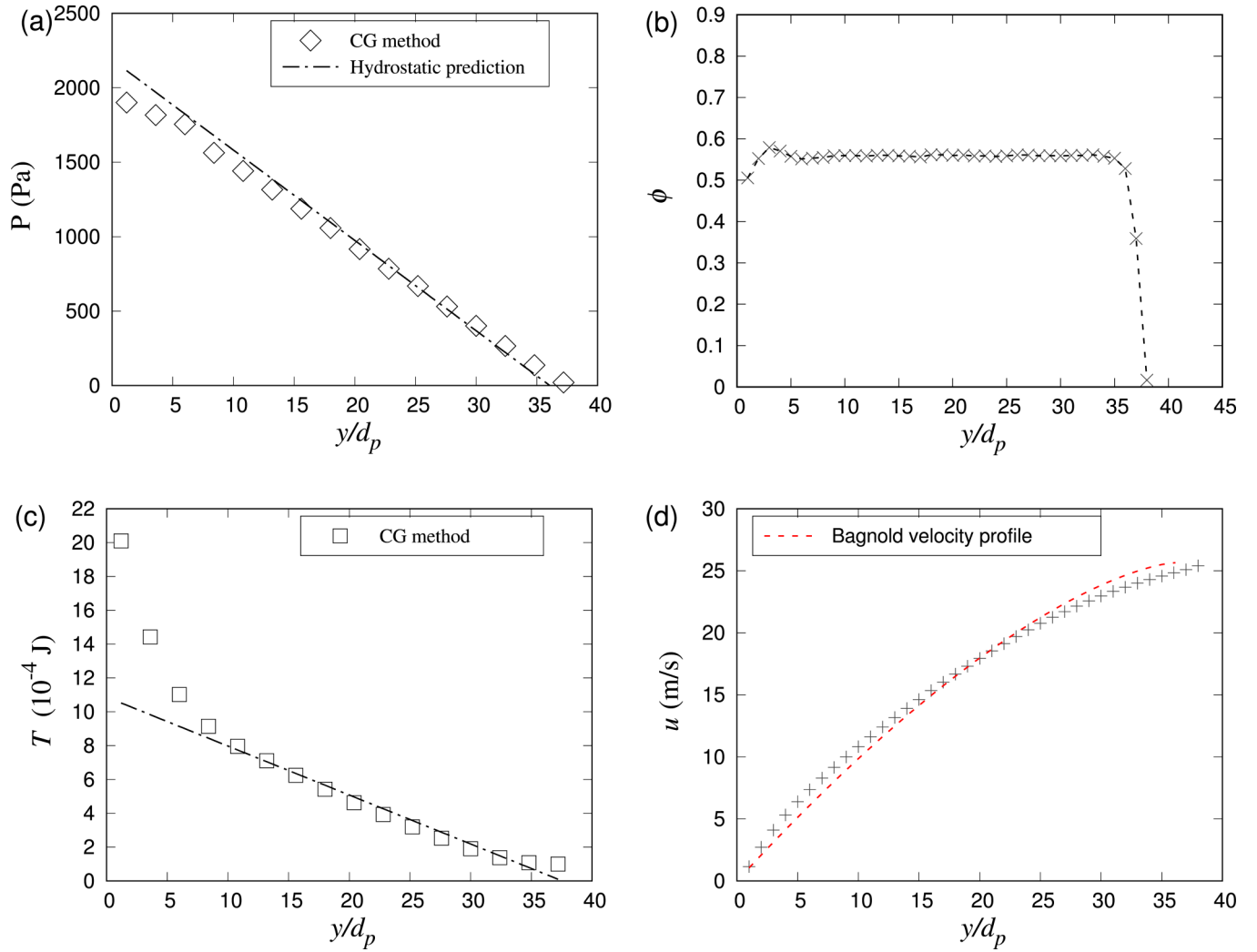
FIG. 5. (a) Granular pressure along the y direction: ($\Diamond$) granular pressure as determined by coarse-graining (CG), (– . –) hydrostatic pressure, i.e., $P_y = \rho_p \phi g_y (h_c - y)$ [Eq. (21)] with $\phi = 0.55$; (b) solid fraction along the y direction. The solid fraction is nearly constant across the bed ($\phi = 0.55$) except in the regions close to the surface and bottom (distances of approximately $5d_p$); (c) ($\square$) granular temperature [Eq. (11)] as determined by CG, (– . –) linear fit of the CG data, suggesting a linearity between T and y [Eq. (23)] in the core region of the dense, granular, shear flow; (d) velocity in the x direction as a function of y/d_p: (+) DEM data and (– – –) Bagnold velocity profile [38], i.e., $u(y) = \frac{2}{3} I_\theta \sqrt{P/(\rho_p d_p)} h_c \{1 - [1 - (y/h_c)]^{1.5}\}$, where $I_\theta = \dot{\gamma} d_p / (P/\rho_p)^{0.5}$ (e.g., in this work $I_\theta = 0.17$ for $\theta = 25°$), P is the pressure at the bottom of the system, and h_c is the height of the shear flow system. All data are extracted from a shear flow system with an inclination angle $\theta = 25°$.

obtain the compressibility coefficient:

$$k_p = \frac{1}{n} \frac{1}{m_p \, g_y(h_c - y)} = \frac{1}{P}. \tag{22}$$

In a steady-state, dense, shear flow system, the solid fraction (and hence also the number density) is constant in the core region [29,39,41] as demonstrated in Fig. 5(b). Following Eq. (12), i.e., $P = nT f(e, \phi)$, the granular temperature is also expected to vary linearly with y in regions where n and ϕ are constant. This behavior is confirmed in Fig. 5(c). It is worth noting that both the granular pressure and temperature, Figs. 5(a) and 5(c), as determined by coarse-graining, deviate from their linear dependences with y close to the bottom wall (i.e., at $y < 5d_p$).

This wall-induced deviation is in agreement with previous reports, e.g., [42]. However, in our work the intruder is placed well away from the bottom plate, and hence the linear relationship of both the granular pressure and temperature with y is assumed to hold. Thus, combining Eqs. (12) and (21) yields

$$T = \frac{P}{n \, f(e, \phi)} = \frac{\rho_p \phi \, g_y(h_c - y)}{n \, f(e, \phi)}. \tag{23}$$

As n, e, ϕ are constant along y (and away from the boundaries), we obtain

$$\frac{\partial T}{\partial y} = \frac{1}{n \, f(e, \phi)} \frac{\partial P}{\partial y} = -\frac{\rho_p \phi \, g_y}{n \, f(e, \phi)}. \tag{24}$$
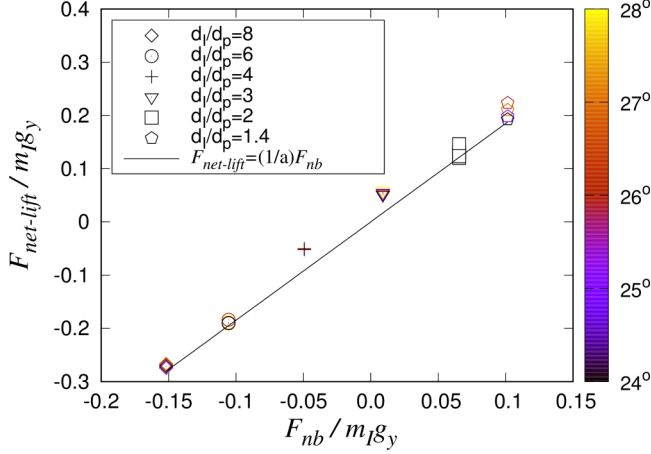
FIG. 6. Linear relationship between the net buoyancy force, F_{nb}, as given by Eq. (28) and the net lift force $F_{\text{net-lift}}$. Each data point represents a DEM simulation of a different d_I/d_p ratio (denoted by the marker symbol) and inclination angle ($\theta = 24°, 25°, 26°, 27°$, and $28°$ denoted by the color scheme). The density ratio $\rho_I/\rho_p = 1$ was used in the simulations.

Rearranging Eq. (24) and combining it with Eq. (23) yields

$$\frac{\partial P}{\partial T} = \frac{\partial P}{\partial y} \bigg/ \frac{\partial T}{\partial y} = n\, f(e, \theta). \tag{25}$$

In addition, from Trujillo and Hermann [13] we have

$$\frac{\alpha}{k_p} = \left(\frac{\partial P}{\partial T} \right)_n. \tag{26}$$

Combining Eqs. (22), (23), and (26) gives

$$\alpha = k_p \left(\frac{\partial P}{\partial T} \right)_n = \frac{1}{P} n\, f(e, \phi) = \frac{1}{T}. \tag{27}$$

Here, following Trujillo and Hermann [13], we have assumed that k_p and α are constant when integrating Eq. (14). Hence, setting $k_p = 1/P_0$ and $\alpha = 1/T_0$, we obtain the following expression for the net buoyancy force acting on the control volume V_c in the reference case [Fig. 4(a)]:

$$F_{nb} = (1 - e^{-\frac{\Delta T}{T_0} + \frac{\Delta P}{P_0}})\rho_p \phi\, g_y V_I. \tag{28}$$

IV. RESULTS AND DISCUSSION

A. Lift force model

In the following, we first establish the correlation between the net lift force $\mathbf{F}_{\text{net-lift}} = -\mathbf{F}_s$ acting on the intruder (i.e., F_s is the spring force that prevents the intruder in the DEM simulations from migrating to the top of the shear flow system) and the derived net buoyancy force acting on the imaginary control volume in Fig. 4(a), i.e., Eq. (28). Figure 6 plots the normalized net lift force on the intruder, $F_{\text{net-lift}}/m_I g_y$, over the normalized net buoyancy force, $F_{nb}/m_I g_y$, for a series of DEM simulations in which the inclination angle and the size ratio d_I/d_p were varied. From Fig. 6 we obtain a linear correlation between $F_{\text{net-lift}}$ and F_{nb}, i.e.,

$$F_{\text{net-lift}} = F_s = \frac{1}{a} F_{nb}, \tag{29}$$

with $a = 0.55 \pm 0.035$. The bulk solid fraction of our shear flow system is $\phi = 0.55$, hence $\phi/a \cong 1$. Substituting Eq. (28) into Eq. (29):

$$F_{\text{net-lift}} = (1 - e^{-\frac{\Delta T}{T_0} + \frac{\Delta P}{P_0}})\rho_p\, g_y V_I. \tag{30}$$

Figure 6 shows that the inclination angle has only a very minor influence on the magnitude of the spring force, in agreement with previous reports [15,17,20]. On the other hand, the size ratio d_I/d_p affects the buoyancy force and hence also the spring force appreciably, i.e., with increasing d_I/d_p the normalized buoyancy force (and the spring force) decrease. To compare our buoyancy model to previously proposed models, we calculate a lift force $\mathbf{F}_{\text{lift}} = -(\mathbf{F}_{\text{net-lift}} + \mathbf{F}_g) = -(\mathbf{F}_{nb}/a + \mathbf{F}_g)$. The lift force is the sum of all forces that act in the opposite direction of gravity on the intruder (e.g., Saffman and buoyancy forces). For our buoyancy model, the lift force in the specific shear system studied here is given by

$$\begin{aligned} F_{\text{lift}} &= |-(\mathbf{F}_{\text{net-lift}} + \mathbf{F}_g)| \\ &= (1 - e^{-\frac{\Delta T}{T_0} + \frac{\Delta P}{P_0}})\rho_p\, g_y V_I + \rho_p\, g_y V_I \\ &= (2 - e^{-\frac{\Delta T}{T_0} + \frac{\Delta P}{P_0}})\, \rho_p\, g_y V_I. \end{aligned} \tag{31}$$

Normalizing the lift force by the gravitational force of the intruder ($\rho_p = \rho_I$) yields

$$\frac{F_{\text{lift}}}{\rho_I\, g_y V_I} = 2 - e^{-\frac{\Delta T}{T_0} + \frac{\Delta P}{P_0}}. \tag{32}$$

In the following, we performed a series of DEM simulations with varying ratios of d_I/d_p, and we determined the lift force acting on the intruder through $\mathbf{F}_{\text{lift}} = -(\mathbf{F}_s + \mathbf{F}_g)$. The differences in the granular pressure and temperature between the reference and the intruder cases, as required for our buoyancy model Eq. (32), were obtained from the Lagrangian DEM data through coarse-graining.

Figure 7 plots the lift force determined by the virtual spring, our proposed buoyancy model [Eq. (32)], the Saffman-based lift force model [Eq. (5)], and the Archimedean-type buoyancy model given by Eq. (7). Concerning the general trend of the lift force, starting from $d_I/d_p = 1$, where $F_{\text{lift}}/(\rho_I V_I g_y) = 1$, the normalized lift force reaches a maximum at $d_I/d_p \sim 1.5$. The existence of a maximum in the (normalized) lift force with d_I/d_p has been observed previously. For example, Guillard et al. [17] observed a maximum in the lift force at $d_I/d_p \sim 2$ in a 2D plane driven shear flow. Similarly, van der Vaart et al. [15] and Jing et al. [20] observed a maximum in the lift force at $d_I/d_p = 1.5$ in a 3D shear chute flow. The reason for the maximum in the lift force is currently unclear, but further below we provide a tentative explanation. For intruder sizes $d_I/d_p > 4$, $F_{\text{lift}}/(\rho_I V_I g_y) < 1$, i.e., the intruder sinks. In several experimental works, the sinking of large intruders ($d_I/d_p > 5$ for $\rho_I/\rho_p = 1$) has been observed, e.g., in rotating cylinders [19,44].

Our lift force model, Eq. (32), predicts the lift force determined by a virtual spring very accurately, while the Archimedean-type buoyancy model [Eq. (7)] of Jing et al. [20] captures the overall trend well but tends to overpredict the DEM data for $d_I/d_p < 6$. The difference between our modeling results and the buoyancy model of Jing et al. [20] is
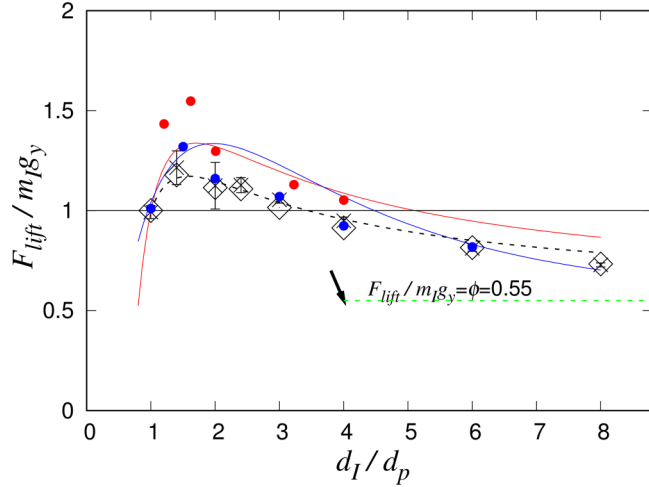
FIG. 7. Normalized lift force as a function of the size ratio d_I/d_p with $\rho_I/\rho_p = 1$: (×) Lift force acting on the intruder as determined directly from the DEM simulations via a virtual spring. The error bars give the standard deviation obtained from five simulations (each 50 s simulation time in the steady state); (◇) lift force as determined by the proposed buoyancy model, i.e., Eq. (32); (——) predictions of the buoyancy model of Jing *et al.* [20], i.e., Eq. (7); (●) inclined shear flow simulation results (Hertzian contact model) of [43]; (——) Saffman force-based lift force model $F_{\text{lift}} = F_{\text{saff}} + F_b = -a_0 b_0 I_\theta \mu^{-0.5}(d_p/d_I - 1)d_I^2 d_p^{-1} s(\dot{\gamma}) + (\phi/\phi_I)\rho_p g_y V_I$ using $a_0 = 0.24$ and $b_0 = 130.0$ as the fitting parameter as given by van der Vaart *et al.* [15]; (●) inclined plane flow simulation results (linear spring-dash contact model) of [15]. The black dashed line is a prediction of Eq. (5) that uses $a_0 = 0.24$ and $b_0 = 93$ as obtained from our simulation data. The solid, horizontal black line is a guiding reference for $F_{\text{lift}}/(\rho_I V_I g_y) = 1$, i.e., below this reference line an intruder sinks, while values above the reference line indicate a rising intruder. (——) Normalized lift force in the continuum limit ($d_I/d_p \gg 1$), i.e., $F_{\text{lift}}/(\rho_I V_I g_y) \rightarrow \phi \sim 0.55$. In the DEM simulations, the inclination angle was varied in the range $\theta = [24°, 28°]$, with $\rho_I/\rho_p = 1$.

likely because the empirical buoyancy model of Jing *et al.* [20] is based on a perfect linear shear system (different from the Bagnold velocity profile obtained in this work). In addition, Fig. 7 includes the lift force data of inclined plane shear flow simulations (Hertzian contact model) [43], which show overall a good agreement with our simulation data. Also, the van der Vaart *et al.* [15] model, Eq. (5), captures very well the overall shape of the lift-force dependency on d_I/d_p, but it also tends to overpredict the DEM data. We speculate that the difference between the simulation results of van der Vaart *et al.* [15] (Hertzian contact model) and our simulation data (linear spring model) is due to the different contact models applied. Indeed, differences in predicted velocity profiles, solid fraction, etc., due to differences in contact models have been reported [24]. When adjusting the fitting parameters of the model of van der Vaart *et al.* [15] to $a_0 = 0.24$ and $b_0 = 93$, a very good agreement with our DEM data is obtained, as illustrated by the dashed line in Fig. 7.

To assess also the dependence of the lift force acting on the intruder on the vertical position of the intruder, the position of the intruder was varied from $y_{\min} = 7d_p$ to $y_{\max} = 34d_p$. According to the velocity profile in the shear flow system
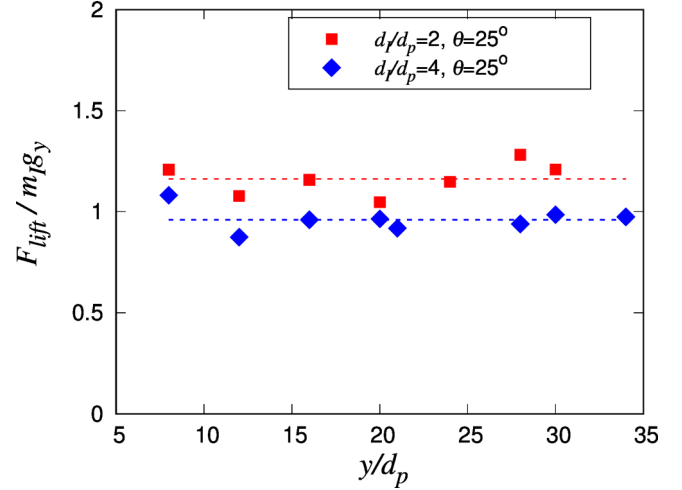

FIG. 8. Lift force acting on the intruder determined directly from the virtual spring as a function of intruder position in the y direction (varied from $y_{\min} = 7d_p$ to $y_{\max} = 34d_p$). From the velocity profile given in Fig. 5(d) the shear rates vary from $186.0\,\text{s}^{-1}$ (at $y = 7d_p$) to $55.5\,\text{s}^{-1}$ (at $y = 34d_p$).

under investigation, Fig. 5(d), the shear rates vary between $186.0\,\text{s}^{-1}$ (at $y = 7d_p$) and $55.5\,\text{s}^{-1}$ (at $y = 34d_p$). Figure 8 shows that the lift force acting on the intruder is not sensitive to the vertical position at which the intruder is placed, suggesting that the lift force acting on the intruder is not sensitive to the shear rate, in agreement with previous observations [15,17,20].

B. Cooling effect of the intruder

To elucidate the contributions of the variations of pressure and temperature field upon the addition of an intruder on the lift force, Fig. 9 plots $\Delta T/T_0$ and $\Delta P/P_0$ as a function of d_I/d_p. We observe that $\Delta T/T_0$ is negative, i.e., the introduction of an intruder leads to a local cooling of the granular temperature. As the ratio d_I/d_p increases, the cooling effect becomes stronger. In the following, we provide a tentative explanation for the cooling effect of the intruder in dense, shear flows. Concerning the granular system at hand, the major contribution to the granular temperature arises from velocity fluctuations along the shear direction x, i.e., $T_x \sim 10^{-5}$ J, $T_y, T_z \sim 10^{-6}$ J for $d_I/d_p = 8$. Hence in the following we focus on the velocity along the x direction. In the reference case, Fig. 10(a), assuming a constant shear rate $\dot{\gamma}_0$ in a coarse-graining (CG) volume, the granular temperature can be written as $T_0 \approx \sum_{y=y_0-w}^{y_0+w}[1/(3N)]m_p\{[\dot{\gamma}_0(y-y_0) + u_0] - u_0\}^2$, where u_0 is the average particle velocity in the CG volume [dashed circle in Fig. 10(a)], N is the number of particles in the coarse-graining volume, m_p is the mass of the bed particles, and y_0 is the vertical position of the center of the CG volume. As $\sum_{y=y_0-w}^{y_0+w}(1/N)[\dot{\gamma}_0^2(y - y_0)^2] = \dot{\gamma}_0^2\langle(y - y_0)^2\rangle$, T_0 can be rewritten as $T_0 \approx (1/3)\dot{\gamma}_0^2 m_p\langle(y - y_0)^2\rangle$, where $\langle\cdot\rangle$ denotes the average operation in the CG volume (located at y_0 with radius w). From Fig. 3(b) we observe that the granular temperature indeed grows quadratically with w, i.e., $T_0 \approx \dot{\gamma}_0^2 w^2$. Hence, two main factors affect the magnitude of granular
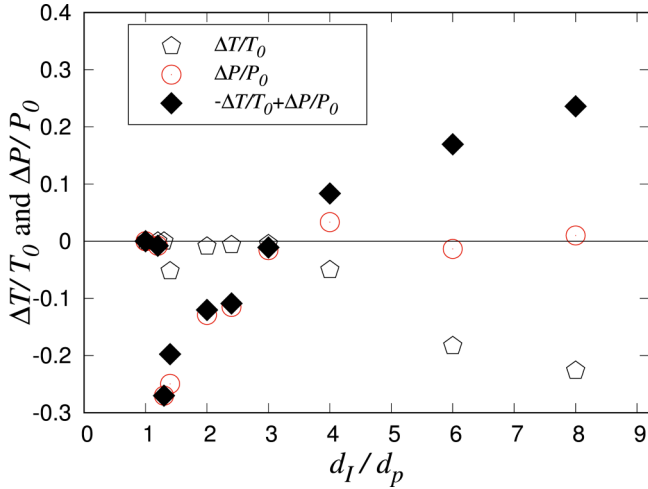
FIG. 9. Variation of $\Delta P/P_0$ ($\Delta P = P_1 - P_0$) and $\Delta T/T_0$ ($\Delta T = T_1 - T_0$) as a function of d_I/d_p. Both the granular pressure and temperature are determined through coarse-graining of the DEM data (simulation performed with an inclination angle $\theta = 25°$ and $\rho_I/\rho_p = 1$). P_0 is the hydrostatic pressure, which could be determined by coarse-graining or analytically [$P_0 = \rho_p g_y(h_c - y_0)$ with $y_0 = 0.1 \, m$].
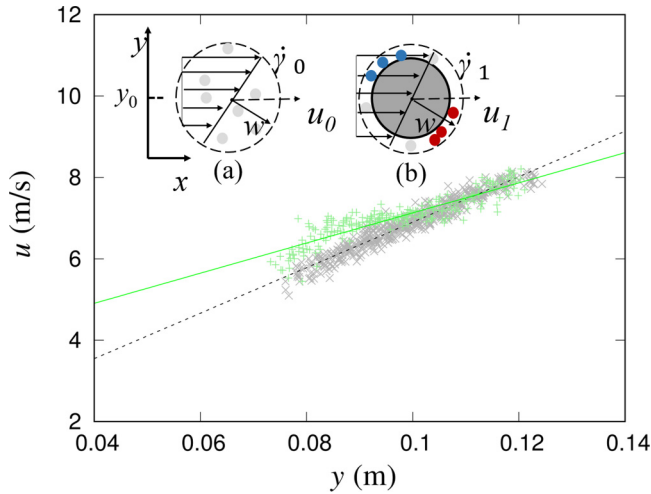

FIG. 10. Velocity (in the shear direction x) of individual particles at $t = 399$ s that are located in the coarse-graining volume centered at $y_0 = 0.1 \, m$. The black dashed circle denotes the CG volume of radius $w = r_I + d_p$ where $r_I = 8d_p$. (×) Particle velocities in the reference case [inset in (a)] with (- - -) fitting assuming a constant shear rate in the CG volume, i.e., $\dot\gamma_0 = 59.5 \, s^{-1}$ (+). Particle velocities in the intruder case [inset in (b)] with (—) being the constant shear rate fitting, i.e., $\dot\gamma_1 = 37.1 \, s^{-1}$ in the CG volume. System parameters are $d_I/d_p = 8$, $\rho_I/\rho_p = 1$, and $\theta = 28°$. Inset (a): coarse-graining (CG) volume of the reference case. The CG volume is a spherical space of radius w. Here, u_0 denotes the average velocity of the particles that are in the CG volume and $\dot\gamma_0$ is the shear rate in the CG volume. Inset (b): CG volume of the intruder case; the dark gray area denotes the intruder, $\dot\gamma_1$ is the shear rate in the CG volume, and u_1 is the average velocity of the particles in the CG volume. The blue particles at the top of the intruder indicate a reduced velocity compared to the reference case, while the red particles at the bottom of the intruder denote faster particles compared to the reference case.

temperature: (i) the size of the CG volume, i.e., w [Fig. 3(b)], and (ii) the magnitude of the shear rate.

Introducing an intruder into the shear system [Fig. 10(b)] affects the average velocity in the coarse-graining volume (new average velocity u_1). Similar to the reference case (assuming again a constant shear rate in the coarse-graining volume), we can write the granular temperature in the intruder case as $T_1 = (1/3)\dot\gamma_1^2 m p \langle(y - y_0)^2\rangle$. Figure 10 plots the velocity of particles (in the shear direction x) for the reference and the intruder case, including fits for the shear rate assuming a constant shear rate in the coarse-graining volume. For the reference and the intruder case, shear rates of $\dot\gamma_0 = 59.5 \, s^{-1}$ and $\dot\gamma_1 = 37.1 \, s^{-1}$ (at $y = 0.1$ m) are obtained, respectively. The shear rate in the intruder case is significantly lower than in the reference case, resulting in a lower granular temperature (cooling) in the intruder case. Overall, it appears that the presence of an intruder leads to a reduced particle velocity at its top and a higher particle velocity at its bottom when compared to the reference case.

As a consequence, we observe that the intruder flattens the velocity profile in the CG volume, which results in an overall cooling effect and hence a negative value of $\Delta T/T_0$ in particular for large intruders. The cooling effect of large intruders as observed in our dense, shear flow system is to some extent in contradiction to the work of Trujillo and Hermann [13], in which the intruder behaves like a heating source in a granular gas. Yet, the system studied in [13] is very different from our system, as it considers a dilute granular gas system under strong vibrations. In the system of Trujillo and Hermann [13], a binary collision dominates (with a long free path length), whereas in our system multiple and enduring contacts prevail.

C. Continuum limit

From Fig. 9 we observe that for $d_I/d_p > 4$, $\Delta P/P_0 \to 0$. This asymptotic behavior of $\Delta P/P_0$ is an indication that for $d_I/d_p \gg 1$ the system approaches a continuum limit, i.e., the lift force acting on the intruder approaches the value given by an Archimedean-type description of the buoyancy force, i.e., $F_b = \phi \rho_p g_y V_I$, or $F_b/\rho_p g_y V_I \to \phi$ (Fig. 7). This trend has also been reported by Jing *et al.* [20] and van der Vaart *et al.* [15]. In the continuum limit, i.e., $d_I/d_p \gg 1$, the intruder behaves as if being immersed in a fluid with density $\rho_p \phi$. Jing *et al.* [20] argued that for $d_I/d_p \gg 1$, a large number of bed particles are surrounding (and hence in contact) with the intruder, leading to a high number of particle collisions and in turn a uniform stress transmission (similar to a continuum fluid). Therefore, for large values of d_I/d_p, $\Delta P = P_1 - P_0$ approaches zero (as confirmed in Fig. 9).

To explore in more depth the change in P when an intruder in the size range $1.5 < d_I/d_p < 4$ is introduced into the system, we calculated the pressure at the location of the intruder over 100 s and plot its distribution as a function of d_I/d_p in Fig. 11. For $d_I/d_p = 1.5$, the modal value of the pressure is 800 Pa (mean value 987 Pa), which is significantly smaller than the hydrostatic pressure of 1153 Pa. The difference between the mean value of the pressure distribution and the hydrostatic pressure is reflected in the positive pressure contribution to the upward-directed lift force acting on intruders with $d_I/d_p < 4$. In addition, the large deviation between the
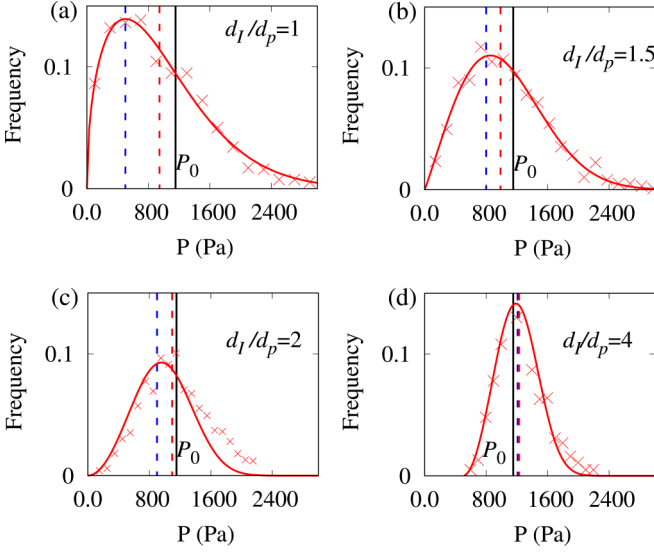
FIG. 11. The distribution of the pressure at the location of the intruder, $P(r(t),t)$, as a function of the size ratio: (a) $d_I/d_p = 1$, (b) $d_I/d_p = 1.5$, (c) $d_I/d_p = 2$, and (d) $d_I/d_p = 4$. The setup used an inclination angle of $\theta = 24°$ with $\rho_I/\rho_p = 1$. Pressure data were sampled over 100 s in steps of 0.1 s. The hydrostatic pressure $P_0 = 1153$ Pa is denoted by the black, solid vertical line, given by $P_0 = \rho_p g_y (h_c - y_0)$ with $h_c = 0.192\,m$ and $y_0 = 0.1\,m$. The mean pressure value is denoted by the red, dashed vertical line. The modal pressure value is denoted by the blue, dashed vertical line: (a) $P_{\mathrm{modal}} = 500$ Pa, $P_{\mathrm{mean}} = 944$ Pa; (b) $P_{\mathrm{modal}} = 800$ Pa, $P_{\mathrm{mean}} = 987$ Pa; (c) $P_{\mathrm{modal}} = 500$ Pa, $P_{\mathrm{mean}} = 1097$ Pa; (d) $P_{\mathrm{modal}} = 1210$ Pa, $P_{\mathrm{mean}} = 1230$ Pa.

modal and hydrostatic pressure is likely the reason for the large fluctuations in the DEM-determined values of the lift force for smaller ratios of d_I/d_p (Fig. 7). Such fluctuations in DEM-determined lift forces have been reported previously [15,17,20]. For $d_I/d_p = 4$, the pressure distribution becomes more symmetric with the modal ($P_{\mathrm{modal}} = 1210$ Pa), mean ($P_{\mathrm{mean}} = 1230$Pa), and hydrostatic ($P_0 = 1153$ Pa) pressures being very close to each other [Fig. 11(d)], explaining both the small lift force and the small fluctuations in the DEM-determined lift force for $d_I/d_p \geqslant 4$ (Figs. 7 and 9). The smaller fluctuations in the DEM-determined lift force for larger values of d_I/d_p are in agreement with previous works [15,17,20].

D. Effect of density differences on segregation

So far, we have only considered cases in which the density of the intruder and the bed particles are equal. From Eq. (31), when scaling the lift force with the intruder weight ($\rho_I g_y V_I$), the following relationship is obtained for $\rho_p \neq \rho_I$:

$$\frac{F_{\mathrm{lift}}}{\rho_I \, g_y V_I} = \left(2 - e^{-\frac{\Delta T}{T_0} + \frac{\Delta P}{P_0}}\right)\frac{\rho_p}{\rho_I}. \tag{33}$$

When $F_{\mathrm{lift}}/(\rho_I V_I g_y) < 1$ the intruder sinks, and for >1 the intruder rises. Similar to the model of Jing *et al.* [20], also Eq. (33) shows a decoupling of the effects of the intruder size and density ratios. Figure 12 plots $F_{\mathrm{lift}}/(m_I g_y)$ as a function of ρ_p/ρ_I for $d_I/d_p = 2$ and 4. Similar results to those in Fig. 12 also occur for $d_I/d_p = 1$, further confirming the model. The
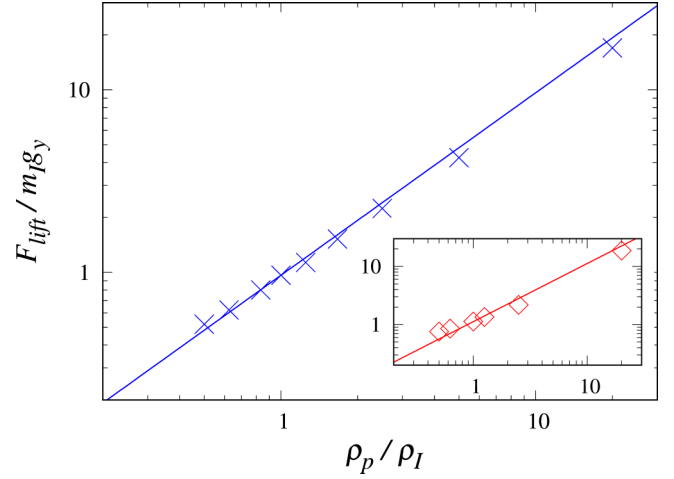

FIG. 12. The normalized lift force as a function of the density ratio ρ_p/ρ_I for different intruder sizes ($\times$) $d_I/d_p = 4$. ($\diamond$) $d_I/d_p = 2$. The blue and red straight lines are Eq. (33).

linear trend predicted by the lift force model, Eq. (33), agrees very well with the DEM data and with experimental observations that show that light intruders migrate upward while heavier intruders sink [19,44], which have been further presented in Fig. 13.

From Eq. (33) it is also possible to extract the neutral buoyancy limit, which is given by $\left(2 - e^{\frac{-\Delta T}{T_0} + \frac{\Delta P}{P_0}}\right)\frac{\rho_p}{\rho_I} = 1$ and plotted in Fig. 13. It is worth noting that the experimental data (solid black symbols) are extracted from multiple intruder systems. For some systems, the neutral buoyancy limit deviates from that of the single intruder simulation results, particularly for size ratios between 1 and 3. It is not surprising, however,
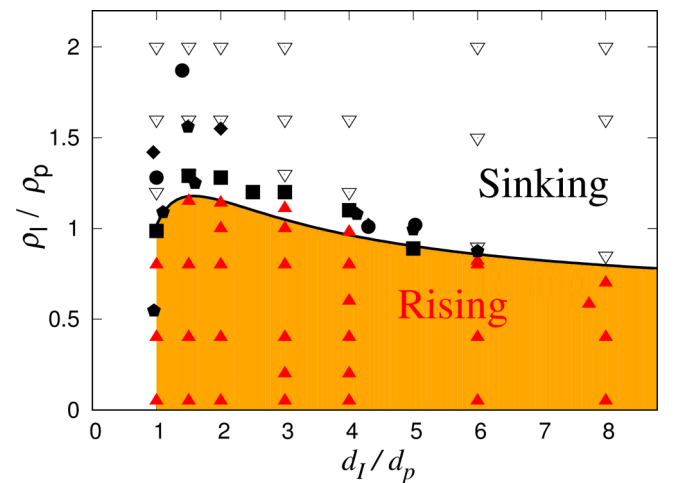

FIG. 13. Neutral buoyancy limit of a single intruder in a dense, granular shear flow as a function of d_I/d_p and ρ_I/ρ_p. The black solid curve denotes the neutral buoyancy limit given by $\left(2 - e^{-\frac{\Delta T}{T_0} + \frac{\Delta P}{P_0}}\right)\frac{\rho_p}{\rho_I} = 1$. DEM data using an inclination angle of $\theta = 25°$. $\triangledown$ intruder sinks, $\blacktriangle$ intruder rises. The solid black symbols are neutral buoyancy limits obtained in ($\blacksquare$) plane shear driven flow [20], ($\bullet$) heap flow, ($\blacklozenge$) chute flow, and ($\pentagon$) rotating drums [44].

that the intruder concentration effects the segregation process; see, e.g., [45].

V. CONCLUSIONS

In this work, we propose a lift force model for intruders in dense, granular shear flows by extending the work of Trujillo and Hermann [13]. The lift force is interpreted as a buoyancy force whereby the density difference arises both from granular temperature and granular pressure contributions. We observe that the presence of an intruder leads to a cooling effect and a local flattening of the shear velocity profile (lower shear rate). For large intruders, i.e., $d_I/d_p > 4$, the local pressure disturbance (and hence contribution to the lift force) is very small as the system approaches a continuum limit, in which the pressure acting on the intruder equals the hydrostatic pressure

of the system. On the other hand, for $1 < d_I/d_p < 4$ the local granular pressure at the location of the intruder is lower than the hydrostatic pressure, leading in turn to a positive lift force. The cooling effect due to the presence of an intruder increases with intruder size, leading ultimately to the sinking of large intruders. The modified model predicts DEM-determined lift forces very well and allows the description of a neutral buoyancy limit.

[1] R. L. Brown, J. Inst. Fuel **13**, 15 (1939).

[2] A. Rosato, K. J. Strandburg, F. Prinz, and R. H. Swendsen, Phys. Rev. Lett. **58**, 1038 (1987).

[3] N. Burtally, P. J. King, and M. R. Swift, Science **295**, 1877 (2002).

[4] G. Lu and C. R. Muller, Granul. Matter **22**, 50 (2020).

[5] K. M. Hill, A. Caprihan, and J. Kakalios, Phys. Rev. E **56**, 4386 (1997).

[6] A. Janda, D. Maza, A. Garcimartin, E. Kolb, J. Lanuza, and E. Clément, Europhys. Lett. **87**, 24002 (2009).

[7] P. Bartelt and B. W. McArdell, J. Glaciol. **55**, 829 (2009).

[8] G. B. Crosta, H. Chen, and C. F. Lee, Geomorphology **60**, 127 (2004).

[9] J. Duran, J. Rajchenbach, and E. Clément, Phys. Rev. Lett. **70**, 2431 (1993).

[10] J. B. Knight, H. M. Jaeger, and S. R. Nagel, Phys. Rev. Lett. **70**, 3728 (1993).

[11] N. Shishodia and C. R. Wassgren, Phys. Rev. Lett. **87**, 084302 (2001).

[12] D. A. Huerta, V. Sosa, M. C. Vargas, and J. C. Ruiz-Suárez, Phys. Rev. E **72**, 031307 (2005).

[13] L. Trujillo and H. J. Herrmann, Physica A **330**, 519 (2003).

[14] T. Shinbrot and F. J. Muzzio, Phys. Rev. Lett. **81**, 4365 (1998).

[15] K. van der Vaart, M. P. van Schrojenstein Lantman, T. Weinhart, S. Luding, C. Ancey, and A. R. Thornton, Phys. Rev. Fluids **3**, 074303 (2018).

[16] S. B. Savage and C. K. K. Lun, J. Fluid Mech. **189**, 311 (1988).

[17] F. Guillard, Y. Forterre, and O. Pouliquen, J. Fluid Mech. **807** (2016).

[18] M. Kiani Oshtorjani, L. Meng, and C. R. Müller, Phys. Rev. E **103**, 062903 (2021).

[19] N. Thomas, Phys. Rev. E **62**, 961 (2000).

[20] L. Jing, J. M. Ottino, R. M. Lueptow, and P. B. Umbanhowar, Phys. Rev. Research **2**, 022069(R) (2020).

[21] C. Kloss, C. Goniva, A. Hager, S. Amberger, and S. Pirker, Progr. Computat. Fluid Dyn. **12**, 140 (2012).

[22] Y. Tsuji, T. Tanaka, and T. Ishida, Powder Technol. **71**, 239 (1992).

[23] D. Antypov and J. A. Elliott, Europhys. Lett. **94**, 50004 (2011).

[24] L. E. Silbert, D. Ertaş, G. S. Grest, T. C. Halsey, D. Levine, and S. J. Plimpton, Phys. Rev. E **64**, 051302 (2001).

[25] I. Goldhirsch, Granul. Matter **12**, 239 (2010).

[26] C. Goldenberg, A. P. F. Atman, P. Claudin, G. Combe, and I. Goldhirsch, Phys. Rev. Lett. **96**, 168001 (2006).

[27] B. Andreotti, Y. Forterre, and O. Pouliquen, *Granular Media: Between Fluid and Solid* (Cambridge University Press, Cambridge, England, 2013).

[28] T. Weinhart, R. Hartkamp, A. R. Thornton, and S. Luding, Phys. Fluids **25**, 070605 (2013).

[29] T. Weinhart, C. Labra, S. Luding, and J. Y. Ooi, Powder Technol. **293**, 138 (2016).

[30] D. R. Tunuguntla, T. Weinhart, and A. R. Thornton, Comput. Part. Mech. **4**, 387 (2017).

[31] P. K. Haff, J. Fluid Mech. **134**, 401 (1983).

[32] B. J. Glasser and I. Goldhirsch, Phys. Fluids **13**, 407 (2001).

[33] H. J. Herrmann, J. Phys. II **3**, 427 (1993).

[34] L. Bocquet, W. Losert, D. Schalk, T. C. Lubensky, and J. P. Gollub, Phys. Rev. E **65**, 011307 (2001).

[35] V. Garzó and J. W. Dufty, Phys. Rev. E **59**, 5895 (1999).

[36] J. T. Jenkins and D. Berzi, Granul. Matter **12**, 151 (2010).

[37] V. Kumaran, C. R. Phys **16**, 51 (2015).

[38] R. A. Bagnold, Proc. R. Soc. London A **225**, 49 (1954).

[39] M. Y. Louge, Phys. Rev. E **67**, 061303 (2003).

[40] J. T. Jenkins and D. K. Yoon, Phys. Rev. Lett. **88**, 194301 (2002).

[41] J. T. Jenkins, Phys. Fluids **18**, 103307 (2006).

[42] T. Weinhart, A. R. Thornton, S. Luding, and O. Bokhove, Granul. Matter **14**, 289 (2012).

[43] L. Jing, J. M. Ottino, R. M. Lueptow, and P. B. Umbanhowar, J. Fluid Mech. **925**, A29 (2021).

[44] G. Félix and N. Thomas, Phys. Rev. E **70**, 051307 (2004).

[45] Y. Duan, P. B. Umbanhowar, J. M. Ottino, and R. M. Lueptow, J. Fluid Mech. **918**, A20 (2021).